Advances in Science and Technology Research Journal

*Advances in Science and Technology Research Journal*, 2026, 20(5), 185–201
https://doi.org/10.12913/22998624/215841
ISSN 2299-8624, License CC-BY 4.0

Received: 2025.10.01
Accepted: 2026.03.15
Published: 2026.04.01

# Microstructural and mechanical characterisation of AA8011 aluminium alloy after tungsten inert gas welding under variable current parameters

Wahyu Dianto[1,2], Fx. Arif Wahyudianto[3*], Agus Suprihanto[2], Rusman[1], Mika Patayang[1]

[1] Department of Maritime Affairs, Samarinda State Polytechnic, Samarinda, 75131, Indonesia
[2] Department of Mechanical Engineering, Diponegoro University, Semarang, 50275, Indonesia
[3] Department of Mechanical Engineering, Samarinda State Polytechnic, Samarinda, 75131, Indonesia
* Corresponding author's e-mail: wahyuaryadillah@gmail.com

## ABSTRACT

AA8011 aluminium alloy is widely used in automotive radiator applications due to its good corrosion resistance, adequate strength, and excellent thermal conductivity. However, its mechanical performance after welding is strongly influenced by the thermal cycle and the heat input during TIG welding. This study investigated the effect of welding current variations (115 A, 120 A, and 125 A) on the post-weld mechanical properties and microstructural evolution of AA8011 alloy. Tensile testing, Vickers microhardness mapping, macro-microstructural observations, and weld-bead geometry evaluation were performed in accordance with the ASTM and AWS standards. Results show that welding current significantly affects grain morphology, hardness distribution, and tensile performance. The optimum mechanical response was obtained at 120 A. The novelty of this work lies in providing a comprehensive mechanical-microstructural characterisation of TIG-welded AA8011 alloy, thereby contributing scientific insights toward the optimisation of welding parameters for lightweight radiator components.

**Keywords:** AA8011 aluminium alloy, TIG welding, welding current, microstructure; mechanical properties, hardness, tensile strength.

## INTRODUCTION

Aluminium alloys are widely utilised in modern engineering applications due to their low density, high thermal conductivity, corrosion resistance, and favourable mechanical performance, making them excellent candidates for lightweight automotive structures and thermal-management components [1]. These advantages also support their use in aluminium die-casting industries, where significant economic considerations drive ongoing improvements in mould performance; the production of complex moulds often requires investments ranging from tens to hundreds of thousands of Euros [2]. These processes – whether electric or gas-shielded – rely on high thermal input, which can compromise weld quality [3]. In advanced thermal-management systems, aluminium is further enhanced through technologies, such as spray cooling, which provides efficient heat dissipation and is widely applied in steel mills, turbines, and high-power electronic systems [4]. Its combination of high specific strength, rigidity, and durability has contributed to the expanding use of aluminium in aerospace, construction, and other industrial sectors [5]. High-strength aluminium alloys strengthened by precipitation – particularly those alloyed with zinc – are frequently used in aircraft structures, armour systems, and heavy-duty transportation components due to their superior mechanical performance [6]. Recent advancements in cooling systems have explored nanoparticle-enhanced and ternary hybrid nanofluids, which significantly improve radiator heat-transfer

efficiency and engine temperature stability [7,8]. This is a critical factor in long-term performance, as microstructural evolution during service may influence mechanical integrity [7]. Despite progress in mini- and micro-channel radiator designs, the thermal-conductivity limitations of traditional coolants such as water and ethylene glycol continue to limit radiator efficiency [9].

|Tungsten inert gas (TIG) welding remains a preferred joining method for aluminium alloys due to its ability to produce clean, high-quality welds with minimal contamination [10]. Welding of similar and dissimilar metals also enables the fabrication of complex engineering assemblies across various industries [10]. However, aluminium is inherently more challenging to weld than steel due to such factors as high thermal/electrical conductivity, rapid solidification, a refractory $Al_2O_3$ surface layer, and relatively low rigidity. Heat input – primarily governed by welding current – plays a crucial role in determining weld bead geometry, grain refinement, precipitation behaviour, and ultimately the mechanical integrity of the welded joint. TIG welding continues to be recognised for its high joint quality, narrow HAZ, minimal distortion, and low defect formation [11]. Standard evaluation typically includes tensile testing, hardness profiling, flexural testing, and microstructural analysis [12]. Key parameters, such as welding current, electrode-to-workpiece distance, and heat input significantly affect weld formation and defect susceptibility (including porosity, coarse-grain growth, and sedimentation) [13,14]. Previous studies on AA5xxx and AA6xxx alloys indicate that excessive heat input can induce grain coarsening and HAZ softening, whereas insufficient heat input leads to incomplete fusion and poor mechanical properties.

AA8011 – classified in the 8xxx aluminium series – contains significant Fe and Si, which form intermetallic compounds that contribute to its strengthening, wear resistance, and corrosion resistance [15]. Fe- and Si-based phases refine the microstructure while enhancing mechanical properties, making the alloy cost-effective compared to other high-strength aluminium grades [16]. AA8011 is widely used in heat-exchanger fins, HVAC ducting, marine cooling systems, and lightweight automotive applications. Prior research shows that material positioning and tool offset are critical factors in minimising defects in friction-stir-welded AA8011 joints [17]. Increasing interest in aluminium for structural applications is reflected in automotive body design, where up to 70–80% of modern vehicle body components consist of aluminium alloys in sheet, extruded, or cast form [18]. Aluminium and its composites are also increasingly employed in aerospace, defence, electronics, and tribological applications due to their customisable reinforcement capabilities. [19]. Modern welding technologies – including the K-TIG method – offer advantages such as high productivity, precision, and cost efficiency [20]. Spectrometric analysis confirms that AA8011 typically comprises Al (~97.856 wt.%), Fe, Si, Mg, Zn, Cu, Mn, Cr, Ti, and minor trace elements [21]. However, AA8011 has been understudied compared with the 5xxx and 6xxx series, particularly regarding TIG welding parameter optimisation, mechanical responses, and microstructural evolution. However, TIG welding parameters are known to exert direct and indirect influences on weld microstructure, mechanical properties, and defect formation [11]. Few studies have investigated how welding current specifically affects AA8011. The absence of research linking heat input to mechanical–microstructural correlations represents a clear gap in the literature.

Another vital aspect is weld groove geometry. Numerous studies demonstrate that groove dimensions (e.g., V-groove, U-groove, square butt) affect thermal distribution, penetration depth, and weld integrity. Although the present study adopts a flat 1G configuration without groove variation, the influence of groove geometry remains a relevant topic for future extension.

On the basis of the above, a significant research gap exists:

1. AA8011 alloy is widely used in automotive radiators yet rarely studied in the TIG-welded condition,
2. The effect of welding current on AA8011 post-weld properties remains insufficiently documented,
3. Quantitative regression-based correlations between heat input and mechanical properties for AA8011 are absent in the literature, and
4. No clear parameter optimisation guidelines exist for TIG welding of 8xxx-series alloys.

Therefore, this study aimed to characterise the influence of TIG welding current variations (115 A, 120 A, 125 A) on the tensile behaviour, hardness distribution, bead geometry, and

microstructural evolution of AA8011 alloy. The novelty of this work lies in providing a systematic mechanical-microstructural correlation supported by experimental evidence, forming a scientific foundation for optimising welding parameters in lightweight radiator applications. This study also provided initial recommendations for selecting the optimal TIG current for AA8011, balancing strength, hardness, and microstructural homogeneity.

## RESEARCH METHOD

This study employed an experimental approach to evaluate the effect of TIG welding current on the mechanical and microstructural characteristics of AA8011 aluminium alloy. Three current levels – 115 A, 120 A, and 125 A – were selected to represent low, medium, and high heat input conditions. All welding, specimen preparation, and mechanical testing procedures were conducted in accordance with relevant international standards to ensure reproducibility and comparability.

### Base material and chemical composition

The base material used in this study was commercial AA8011 aluminium sheet (3 mm thick), commonly used for radiator fins and heat exchanger components. Optical emission spectrometry (OES) confirmed the chemical composition as Al – 97.856%, Fe – 0.901%, Si – 0.375%, Zn – 0.209%, Mg – 0.374%, Cu – 0.157%, Mn – 0.111%, Cr – 0.009%, Ti – 0.005%, and trace elements. The high Fe–Si content provides dispersion-strengthened characteristics typical of the 8xxx aluminium series.

### Welding procedure

TIG welding was performed in a flat 1G position using ER4043 filler wire (Al–Si alloy, Ø 2.4 mm). The welding process followed the general guidelines of AWS D1.2/D1.2M (structural welding code – aluminium) to ensure proper joint preparation, gas shielding, arc control, and bead formation. This method operates on the principle that the thermal conditions in the weld area are directly related to the evolution of the microstructure, which in turn determines the mechanical properties of the weld. Predictive models enable real-time adjustment of welding parameters to achieve optimal mechanical properties, thereby improving welding efficiency and reliability [22]. This study examined the impact of three arc current levels on the mechanical properties of the TIG welding process, specifically, hardness and tensile strength [11].

Variable parameter: welding current

- 115 A → low heat input
- 120 A → medium/optimal heat input
- 125 A → high heat input

These current levels were chosen based on preliminary trials and common TIG operating ranges for 3-mm AA8xxx materials. The initial method used was TIG welding, in which an electric arc is formed between the unused tungsten electrode and the metal plate [22] (Table 1).

### Specimen preparation

All welded plates were sectioned using a precision cutter. Mechanical test specimens were prepared according to the following standards:

- tensile test: ASTM E8/E8M,
- hardness test (Vickers microhardness): ASTM E92,
- microstructure etching: ASTM E407,
- macrostructure observation: ASTM E340.

The tensile specimens were machined into sub-size samples with a 50 mm gauge length. Hardness mapping was performed across the weld metal (WM), heat-affected zone (HAZ), and base metal (BM) at 1 mm spacing, totalling 31 measurement points.

**Table 1.** Welding parameters (constant unless stated otherwise)

| Parameter | Value |
|---|---|
| Welding process | TIG (GTAW) |
| Filler metal | ER4043, Ø2.4 mm |
| Polarity | AC (alternating current) |
| Shielding gas | 99.99% Argon |
| Gas flow rate | 12–15 L/min |
| Welding speed | 120 mm/min (constant) |
| Electrode type | 2% thoriated tungsten |
| Electrode tip angle | 60° |
| Torch angle | 15° push angle |
| Joint configuration | Square butt joint (no groove), 1G |

### Tensile testing

Tensile testing was performed using a 50 kN universal testing machine. The crosshead speed was set to 1 mm/min. Yield strength (YS), ultimate tensile strength (UTS), and elongation were automatically recorded. Three specimens were tested for each current level, and average values were computed. Testing complied with all requirements of ASTM E8/E8M, including parallelism, gauge length marking, and fracture mode classification.

### Hardness testing

Microhardness was measured using a Vickers indenter under a 100 gf (0.1 kgf) load with a dwell time of 10 seconds. Indentation points covered:

- 10 points BM,
- 10 points HAZ,
- 11 points WM.

The hardness profile provides insight into softening behaviour, grain refinement, and thermal influence across zones.

### Metallographic preparation and microstructural analysis

Metallographic samples were ground using SiC papers (240–2500 grit), polished with 1 µm alumina suspension, and etched with Keller's reagent per ASTM E407. Microstructure analysis included:

- grain morphology (coarse/fine, equiaxed/columnar),
- intermetallic particle distribution,
- boundary segregation characteristics,
- image analysis (ImageJ) for: grain size, phase fraction percentage, ECD (equivalent circular diameter) distribution.

Macrostructure analysis (bead geometry: height, width, penetration) followed ASTM E340.

### Weld bead geometry measurement

Weld bead height and width were measured using digital microscopy. The estimated reinforcement area was calculated using a semi-elliptical approximation:

$$A \approx \pi 4\,(h \times w)\,A \qquad (1)$$

This provides a quantitative comparison of the effects of metal deposition and heat input.

### Data analysis and statistical evaluation

#### *Multivariate regression analysis*

A multiple linear regression model was constructed to evaluate relationships between:

- welding current (A),
- weld bead geometry (height, width),
- hardness (BM–HAZ–WM),
- tensile properties (UTS, YS, elongation).

General form:

$$Y = \beta 0 + \beta 1 I + \beta 2 H + \beta 3 W + \beta 4 HVWM + \epsilon \quad (2)$$

where: $Y$ – mechanical property (UTS or YS), $I$ – current, $H$ – bead height, $W$ – bead width, $HV\_WM$ – microhardness of weld metal.

Regression analysis allows the identification of dominant factors controlling strength.

#### *Process optimisation approach*

Although this study focuses on empirical experiments, optimisation principles were incorporated to align with best practices:

- response surface methodology (RSM) for trend prediction,
- teaching–learning-based optimisation (TLBO) (Baghel, 2025),
- Cuckoo search algorithm for parameter tuning
- heat input–grain size correlation models (Hall–Petch basis).

These frameworks serve as the foundation for future predictive models and further parametric optimisation studies.

## RESULTS AND DISCUSSION

In the welding process for AA8011 aluminium, the radiator material uses three current settings: 115 A, 120 A, and 125 A, with ER4043 electrodes and flat welding (1G), as shown in the Table 2. A picture of the result of welding can be seen in Figure 1(a) 115 A, (b) 120 A, and (c) 125 A. The following is a detailed analysis of the side appearance of the TIG weld on AA8011 (t = 3 mm) with filler ER4043, Ø2.4 mm, based on the reinforcement height and the bead width. The results of the weld measurement are in Table 2.

The estimated area of the amplifier cross-section was calculated from a semi-elliptical approach: A≈π4 W H. Useful as an indicator of the relative amount of deposition/convection metal (assuming

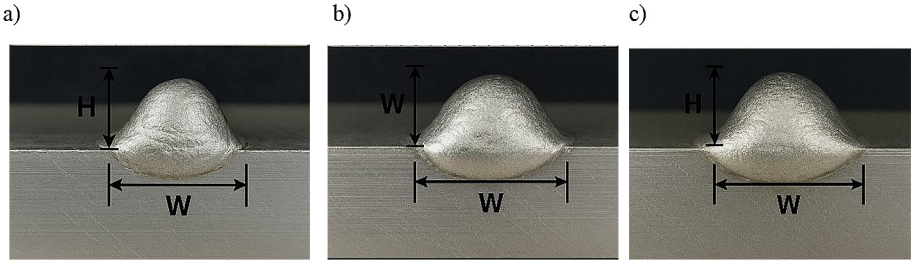


**Figure 1.** The general top-view appearance of the welds: (a) 115 A, (b) 120 A, (c) 125 A

**Table 2.** Weld bead geometry

| Current (A) | Height (mm) | Width (mm) | H/W Ratio | Estimated area (mm²) |
|---|---|---|---|---|
| 115 | 0.30 | 7.90 | 0.038 | 1.86 |
| 120 | 0.60 | 8.60 | 0.070 | 4.05 |
| 125 | 0.40 | 9.20 | 0.043 | 2.89 |

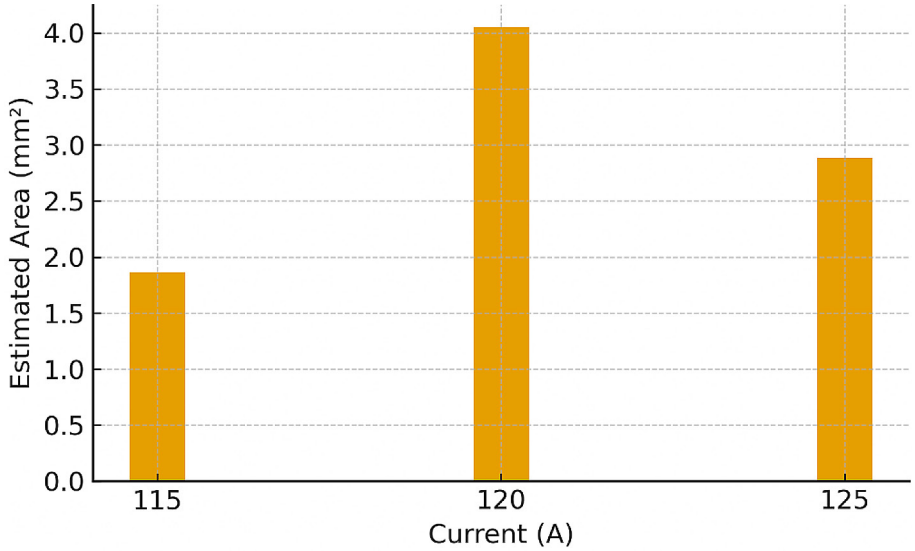


**Figure 2.** Estimated weld bead area vs current

constant velocity of motion). Bead width rises continuously: 7.9 → 8.6 → 9.2 mm (+16.5% from 115 A to 125 A). The amplifier height peaked at 120 A (0.6 mm) and then dropped to 125 A (0.4 mm). The highest H/W (convection) ratio at 120 A is sufficient for wetting, but there is still an amplifier. Bead width increases with current due to higher heat input and fluidity. Maximum reinforcement height occurs at 120 A, indicating optimal melting and deposition. The reinforcement area is highest at 120 A, matching the strongest mechanical response of the weld. This confirms that 120 A produces a more stable weld pool, yielding balanced penetration and bead formation.

The bar chart provides a clear visualisation of how welding current affects weld-bead geometry during TIG welding of AA8011 aluminium alloy. The findings can be summarised as follows:

1. 120 A is the optimal current, producing the most desirable weld bead area.
2. 115 A yields a small bead area due to low heat input and insufficient melting.
3. 125 A results in a decreased area compared to 120 A because of excessive heat input, causing molten pool instability.

These outcomes are consistent with the established TIG welding principles, in which precise

heat control is critical for achieving an ideal weld bead morphology.

The tensile test results indicate that welding with a current of 120 A yields the highest tensile strength, outperforming both 115 A and 125 A. This finding suggests that welding currents below or above the optimal threshold tend to diminish mechanical performance, particularly when the applied current exceeds the ideal range [23]. Overall, the results demonstrate that increasing the welding current generally enhances tensile strength but reduces ductility, which aligns with the typical behaviour of aluminium alloys under elevated heat input. However, a higher current does not necessarily ensure superior weld quality, as other parameters – such as welding speed and arc voltage – jointly influence the magnitude and distribution of heat input within the weld zone [24]. Consequently, the selection of welding current must balance strength and ductility to achieve optimal joint performance. The welded specimens exhibited reductions in both tensile strength and ductility compared with the base material, a trend commonly reported for aluminium welds [25]. If the heat input falls below the minimum required, the fusion between the filler metal and the base material is insufficient, resulting in weak bonding. Conversely, excessive heat input promotes abnormal grain growth, which negatively affects mechanical properties, including tensile strength [26]. Variations in grain size within HAZ significantly influence the mechanical behaviour of the material; coarse grains tend to reduce both strength and ductility, compromising overall joint integrity [27]. The findings of this study confirm the presence of an optimal heat input range for TIG welding AA8011 aluminium alloy. Heat input below this range results in inadequate penetration and insufficient dilution, whereas heat input above this limit promotes excessive grain coarsening and HAZ widening, ultimately reducing tensile strength [28]. These results contribute valuable data by addressing existing gaps in the literature regarding the post-weld mechanical response of AA8011, thereby supporting better parameter selection for industrial welding applications.

The Vickers hardness test was conducted at 31 measurement points, each spaced 1 mm apart. These points consisted of 11 in the weld metal, 10 in the heat-affected zone (HAZ), and 10 in the base metal. The hardness profile obtained from these measurements shows a decline across the HAZ. At the same time, the weld metal exhibits an increase, with the most favourable values recorded at a welding current of 120 A. Previous studies on AA4043 aluminium alloy – using variations in welding current, voltage, and travel speed – have demonstrated that adjustments in welding current significantly influence microhardness, impact toughness, and microstructural evolution within both the weld metal and HAZ regions [27]. Consistent with these findings, the present study confirms that variations in welding current during TIG welding result in notable differences in grain morphology, weld zone geometry, and mechanical performance. An increase in welding current results in a higher heat input, which subsequently induces substantial changes in the microstructure and alters the mechanical characteristics of the material [28]. Therefore, welding current plays a crucial role in determining the quality of welded joints, affecting not only the mechanical response but also the microstructural integrity across the weldment.

Microstructure analysis revealed finer grains at 120 A, than at low or high currents. The photomicrograph results are shown in Figure 3. Photomicro welding BM, HAZ, WM Zone. 115 A. Figure 4. Photomicro welding BM, HAZ, WM Zone. 120 A. Figure 5. Photomicro welding BM, HAZ, WM Zone. 125 A (Table 3).

The progression from 115 A → 120 A → 125 A reflects how heat input governs nucleation, grain growth, and intermetallic distribution:

- At 115 A, limited heat input prevents complete homogenisation of the weld pool, resulting in moderately fine but inconsistent grains.
- At 120 A, the thermal cycle produces rapid nucleation, controlled grain growth, and a uniform Fe–Si intermetallic distribution, generating the most refined microstructure.
- At 125 A, excessive heat causes localised grain coarsening and HAZ widening, slightly reducing structural uniformity.

This microstructural trend is entirely consistent with the mechanical test results. The 120 A weld, which exhibited the finest grain morphology, also delivered the highest UTS, YS, and weld-metal hardness, confirming that grain refinement and controlled thermal input are key determinants of weld performance in AA8011. These microstructural transitions align with established principles of aluminium welding, in which heat input governs nucleation rates, diffusion, and subsequent grain evolution [28]. Furthermore, the introduction of active flux alters the heat transfer

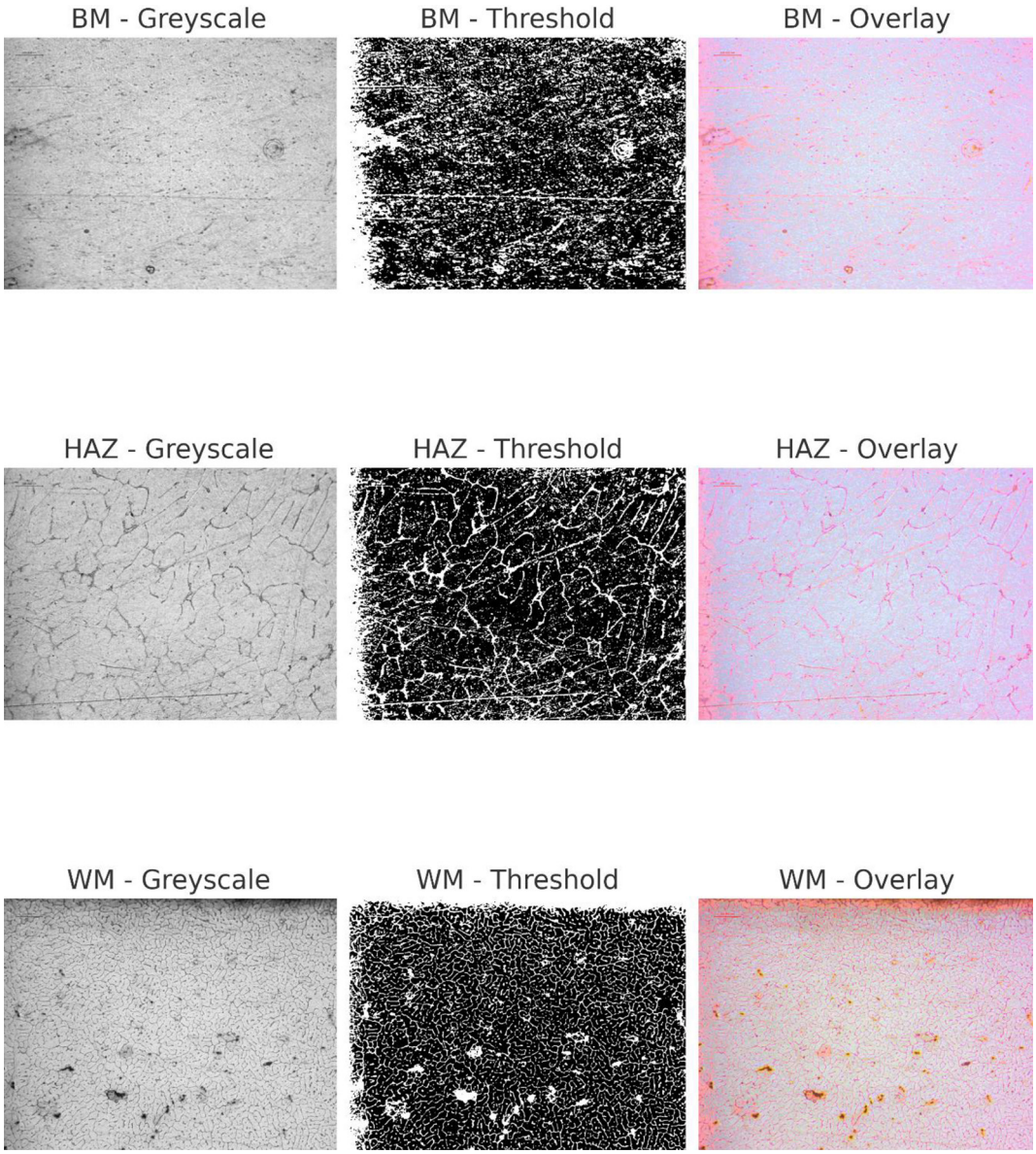


**Figure 3.** Photomicro welding BM, HAZ, WM Zone. 115 A

pattern, influencing the extent of recrystallisation in the HAZ and affecting the hardness and tensile strength of the welded joint. The findings emphasise that the combined effect of welding current and flux selection is crucial for achieving desirable mechanical and microstructural performance in AA8011 [29].

During the tensile test, all specimens were analysed, and the test results were discussed and presented. Tensile testing was carried out on all current variations, which later provided the values for ultimate tensile strength and yield strength. The results of the tensile test are illustrated in Figure 6(a) 115 A, (b) 120 A, (c) 125 A, and the results of the tensile test calculation are in Table 4. A comparison of the mechanical properties of each specimen is shown in Figure 7.

The tensile test results indicate that welding at 120 A produces the highest average tensile strength (UTS) and yield strength (YS) among the tested parameters. This confirms the presence of an optimal current, where mechanical performance improves with increasing current up to a critical point, after which excessive heat input leads to a decline in strength and weld quality [30]. The superior performance at 120 A correlates with the photomicrographic observations showing finer grain structures, consistent with the Hall–Petch relationship, which states that smaller grains enhance both UTS and YS. At 120 A, the material exhibits the lowest elongation (≈3.7%), reflecting

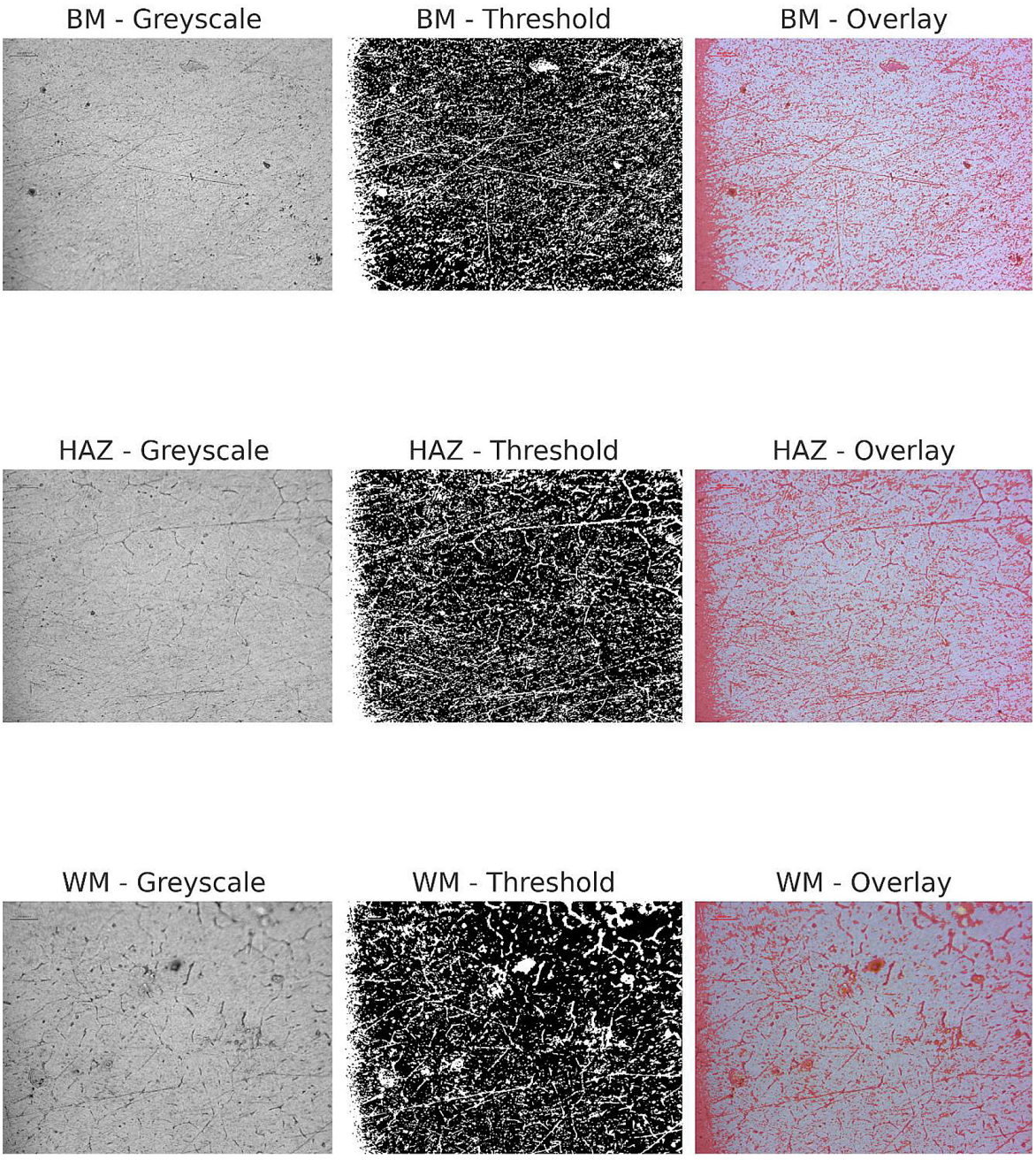


**Figure 4.** Photomicro welding BM, HAZ, WM Zone. 120 A

**Table 3.** Microstructure segmentation summary

| Current | Zone | Al Matrix (%) | Fe–Si (%) | Grain size | Characteristics |
|---|---|---|---|---|---|
| 115A | BM | ~87.2 | ~12.8 | Coarse | Large grains, dispersed precipitates |
| 115A | HAZ | ~88–90 | ~10–12 | Medium | Recrystallised transition region |
| 115A | WM | ~87.4 | ~12.6 | Fine | Rapid solidification, fine grains |
| 120A | BM | ~87.9 | ~12.1 | Coarse | Unaffected base structure |
| 120A | HAZ | ~87.8 | ~12.2 | Medium | Grain refinement transition |
| 120A | WM | ~89.9 | ~10.1 | Finest | Best homogeneity, strongest region |
| 125A | BM | ~88–89 | ~11–12 | Coarse | Similar to BM in 115 A |
| 125A | HAZ | ~88 | ~12 | Medium | Partial recrystallisation |
| 125A | WM | ~89–90 | ~10–11 | Fine | Fine grains but slight overheat segregation |

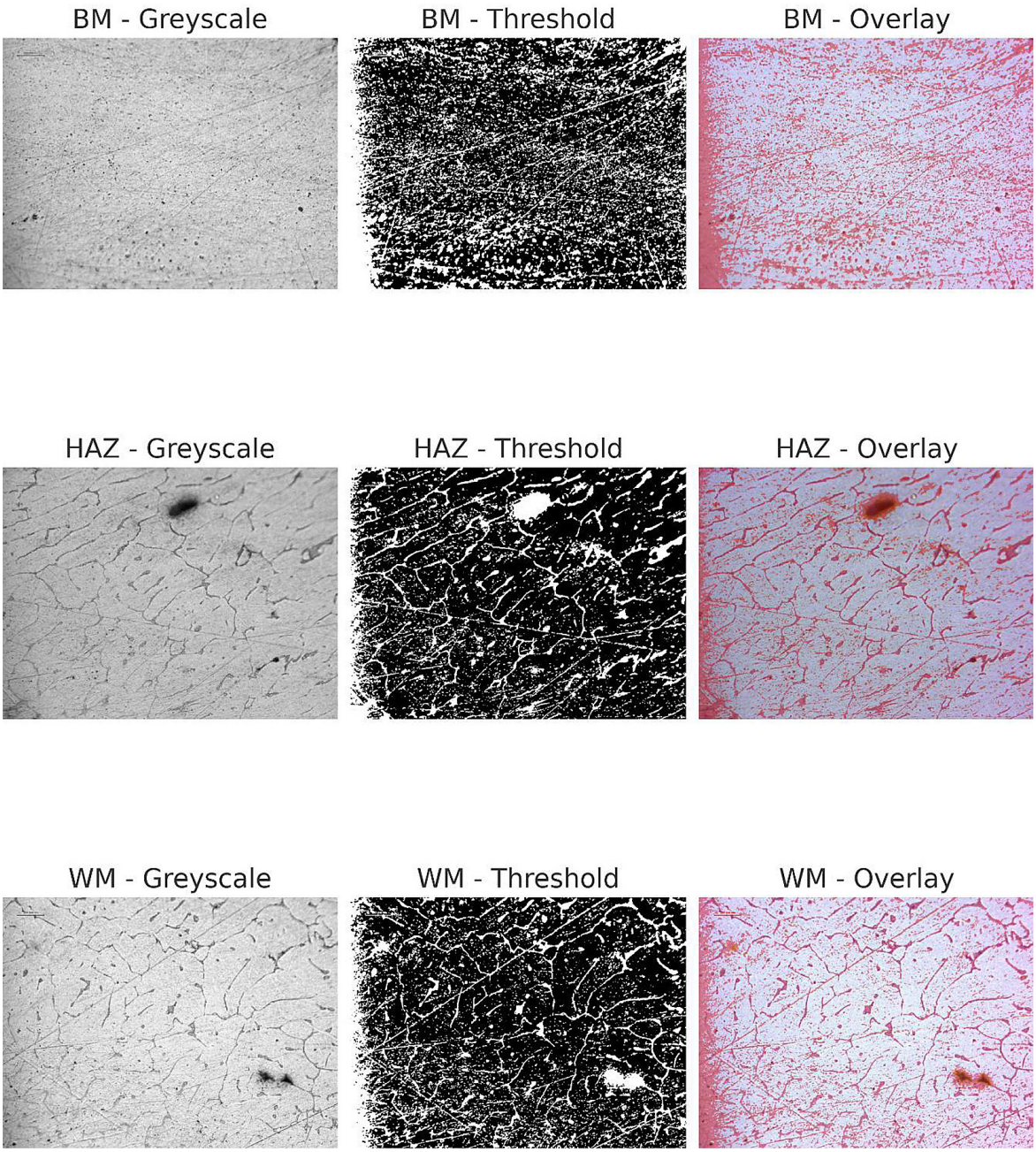


**Figure 5.** Photomicro welding BM, HAZ, WM Zone. 125 A

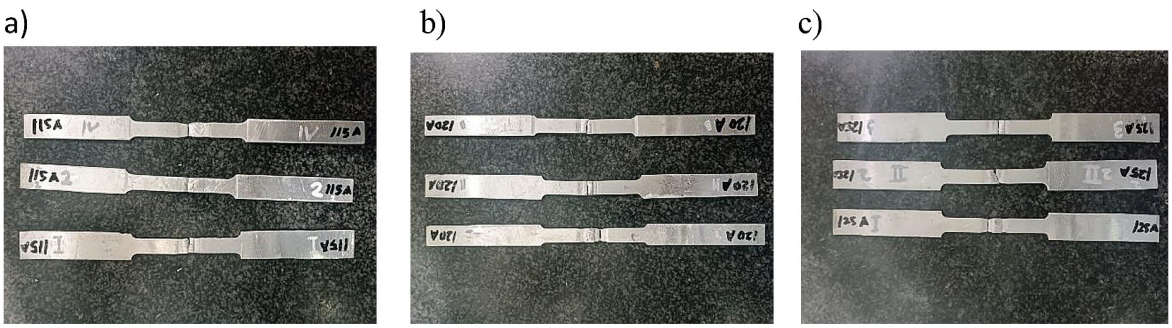


**Figure 6.** Specimen after tensile test a) 115 A, b) 120 A, c) 125 A

**Table 4.** Tensile test result

| Current | UTS (MPa) | YS (MPa) | Elongation (%) |
|---|---|---|---|
| 115 A | 103.14 | 47.62 | 7.33 |
| 120 A | 118.30 | 79.68 | 3.66 |
| 125 A | 112.40 | 63.04 | 5.00 |

a typical trade-off between strength and ductility. In contrast, the 115 A specimen shows the highest elongation (~7%) but also the lowest UTS and YS, indicating a more ductile yet weaker joint. This behaviour is likely influenced by coarser, partially columnar grains and by the presence of softer regions within HAZ. The 125 A condition yields intermediate behaviour, with slightly reduced strength compared with 120 A (UTS ≈112 MPa) and moderate elongation (~5%). The reduction in strength at 125 A may be attributed to grain coarsening or overheating, both of which degrade the load-bearing capacity of the weld. Although the comparative reference study used GMAW, rather than TIG, the underlying metallurgical principles remain analogous: increasing current increases heat input, intensifying thermal exposure within the HAZ. Excessive heat input can deteriorate joint performance due to microstructural changes – such as grain coarsening, phase alteration, or residual-stress-induced cracking – that compromise mechanical integrity [31].

Hardness testing was conducted to evaluate the effect of variations in welding current on the mechanical properties of AA8011 aluminium alloy. This hardness test is illustrated in Figure 8, which shows the hardness test scheme. The observed parameters were the Vickers hardness (HV) values in three areas, namely base metal (BM), heat affected zone (HAZ), and weld metal (WM). The hardness test results are presented in Tables 5, 6, and 7: Average Vickers Hardness for Each Zone. Show Average Results of Hardness Test for Each Current Variation. The results of the violence are shown in Figure 9, which illustrates the hardness values of the current variation.

On the basis of the results presented in Tables 7, 8 and Figure 10, a welding current of 120 A provides the most favourable hardness distribution across the weldment. The BM maintains a stable hardness of approximately 40.67 HV, while HAZ – although showing a reduction – does not exhibit values lower than those recorded at other currents. The WM shows the most pronounced improvement, reaching 43.69 HV, indicating a stronger, more homogeneous microstructure that resists localised deformation more effectively than the welds produced at 115 A and 125 A. At 115 A, WM exhibits a noticeably lower hardness due to insufficient heat input, limiting fusion and grain refinement. Conversely, at 125 A, the WM hardness approaches that of BM, while HAZ shows the greatest softening, indicating that excessive heat input results in thermal overexposure and microstructural degradation. In contrast, the 120 A condition achieves an optimal balance of heat input, cooling rate, and penetration, producing a more uniform hardness profile across BM, HAZ, and WM. Welding speed and current are closely interdependent; therefore, precise current adjustment is

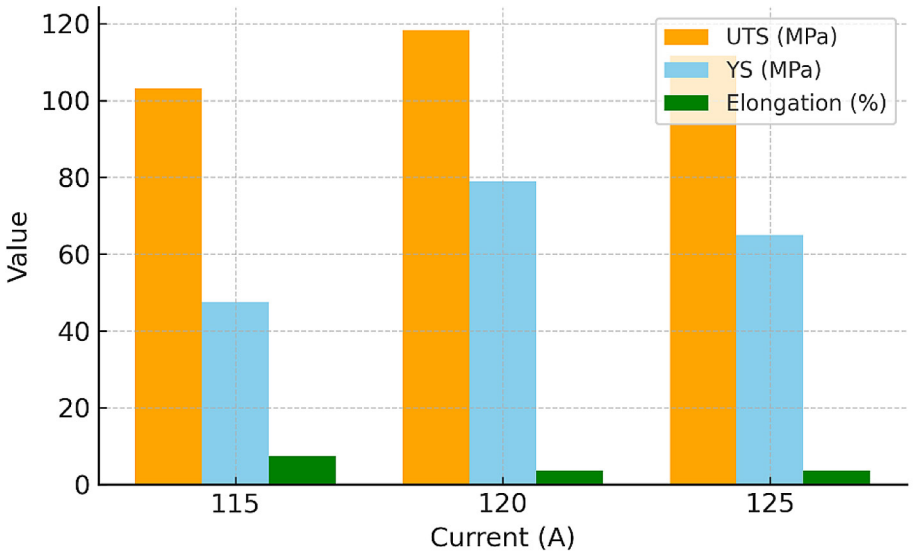


**Figure 7.** Comparison of mechanical properties

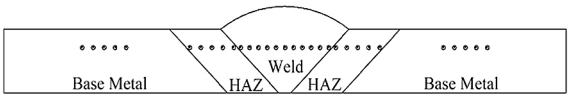


**Figure 8.** Hardness test scheme

essential to maintain an optimal balance among strength, ductility, and microstructural uniformity [32]. When the heat input exceeds the recommended range, grain growth in HAZ intensifies, leading to a decline in joint performance [33].

A welding current of 120 A can therefore be recommended as the optimal parameter for achieving superior strength, hardness, and microstructural homogeneity in 8xxx-series aluminium alloys. Recent research emphasises that the highest current does not necessarily produce the best weld quality; instead, performance is maximised at an optimal current, which is influenced by welding speed, current mode, and shielding gas flow. At this optimum point, the weld exhibits higher strength, stable hardness, and a more uniform microstructure. The findings of this study are consistent with previous reports [30]. Highlighting that appropriate current selection minimises microstructural disparities across the weldment, reduces cracking susceptibility, and enhances overall mechanical resistance.

A multivariate regression approach was employed to quantitatively evaluate how several welding-related variables collectively influence the tensile strength of TIG-welded AA8011 joints.

**Table 5.** Average Vickers hardness 115 A

| Current | No. | D1 (um) | D2 (um) | D (mm) | P (Kgf) | HV |
|---|---|---|---|---|---|---|
| 115A | -15 | 67.43 | 67.54 | 0.067485 | 0.1 | 40.7 |
| | -14 | 67.20 | 68.33 | 0.067765 | 0.1 | 40.4 |
| | -13 | 71.14 | 66.45 | 0.068795 | 0.1 | 39.2 |
| | -12 | 70.79 | 67.27 | 0.06903 | 0.1 | 38.9 |
| | -11 | 71.29 | 71.64 | 0.071465 | 0.1 | 36.3 |
| | -10 | 72.61 | 72.57 | 0.07259 | 0.1 | 35.2 |
| | -9 | 76.01 | 76.57 | 0.07629 | 0.1 | 31.9 |
| | -8 | 73.81 | 75.68 | 0.074745 | 0.1 | 33.2 |
| | -7 | 75.16 | 75.47 | 0.075315 | 0.1 | 32.7 |
| | -6 | 73.31 | 62.4 | 0.067855 | 0.1 | 34.9 |
| | -5 | 73.82 | 73.99 | 0.073905 | 0.1 | 34.0 |
| | -4 | 74.26 | 72.59 | 0.073425 | 0.1 | 34.4 |
| | -3 | 73.31 | 73.8 | 0.073555 | 0.1 | 34.3 |
| | -2 | 63.5 | 63.15 | 0.063325 | 0.1 | 46.2 |
| | -1 | 62.75 | 63.18 | 0.062965 | 0.1 | 46.8 |
| | 0 | 62.31 | 62.24 | 0.062275 | 0.1 | 47.8 |
| | 1 | 65.03 | 65.03 | 0.06503 | 0.1 | 45.1 |
| | 2 | 73.71 | 74.68 | 0.074195 | 0.1 | 33.7 |
| | 3 | 76.01 | 76.22 | 0.076115 | 0.1 | 32.0 |
| | 4 | 76.28 | 79.6 | 0.07794 | 0.1 | 30.5 |
| | 5 | 76.96 | 76.84 | 0.0769 | 0.1 | 31.4 |
| | 6 | 76.51 | 73.84 | 0.075175 | 0.1 | 32.8 |
| | 7 | 79.96 | 74.75 | 0.077355 | 0.1 | 31.0 |
| | 8 | 74.08 | 74.08 | 0.07408 | 0.1 | 33.3 |
| | 9 | 73.28 | 73.228 | 0.073254 | 0.1 | 34.5 |
| | 10 | 69.71 | 69.71 | 0.06971 | 0.1 | 38.0 |
| | 11 | 71.14 | 66.45 | 0.068795 | 0.1 | 39.2 |
| | 12 | 70.78 | 67.26 | 0.06902 | 0.1 | 38.9 |
| | 13 | 67.25 | 68.22 | 0.067735 | 0.1 | 40.4 |
| | 14 | 67.44 | 67.53 | 0.067485 | 0.1 | 40.7 |
| | 15 | 67.98 | 65.44 | 0.06671 | 0.1 | 41.3 |

**Table 6.** Average Vickers hardness 120 A

| Current | No. | D1 (um) | D2 (um) | D (mm) | P (Kgf) | HV |
|---|---|---|---|---|---|---|
| 120 A | -15 | 65.13 | 65.68 | 0.065405 | 0.1 | 43.4 |
| | -14 | 66.43 | 65.54 | 0.065985 | 0.1 | 42.9 |
| | -13 | 67.20 | 66.33 | 0.066765 | 0.1 | 41.4 |
| | -12 | 70.14 | 65.45 | 0.067795 | 0.1 | 40.7 |
| | -11 | 70.79 | 65.27 | 0.06803 | 0.1 | 39.7 |
| | -10 | 71.14 | 66.45 | 0.068795 | 0.1 | 39.2 |
| | -9 | 70.79 | 67.27 | 0.06903 | 0.1 | 38.9 |
| | -8 | 76.81 | 76.68 | 0.076745 | 0.1 | 31.5 |
| | -7 | 75.38 | 75.3 | 0.07534 | 0.1 | 32.7 |
| | -6 | 75.15 | 73.27 | 0.07421 | 0.1 | 33.7 |
| | -5 | 74.24 | 74.24 | 0.07424 | 0.1 | 33.8 |
| | -4 | 71.29 | 71.64 | 0.071465 | 0.1 | 36.3 |
| | -3 | 73.62 | 71.11 | 0.072365 | 0.1 | 35.4 |
| | -2 | 69.71 | 69.71 | 0.06971 | 0.1 | 38.0 |
| | -1 | 63.3 | 65.54 | 0.06442 | 0.1 | 44.7 |
| | 0 | 58.01 | 57.5 | 0.057755 | 0.1 | 55.6 |
| | 1 | 62.04 | 58.28 | 0.06016 | 0.1 | 51.2 |
| | 2 | 62.59 | 63.11 | 0.06285 | 0.1 | 46.9 |
| | 3 | 64.19 | 65.13 | 0.06466 | 0.1 | 44.4 |
| | 4 | 67.43 | 67.54 | 0.067485 | 0.1 | 40.7 |
| | 5 | 70.79 | 67.27 | 0.06903 | 0.1 | 38.9 |
| | 6 | 74.75 | 75.32 | 0.075035 | 0.1 | 32.9 |
| | 7 | 75.86 | 75.53 | 0.075695 | 0,1 | 32.4 |
| | 8 | 76.26 | 75.86 | 0.07606 | 0.1 | 32.1 |
| | 9 | 73.38 | 72.81 | 0.073095 | 0.1 | 34.7 |
| | 10 | 70.61 | 67.42 | 0.069015 | 0.1 | 38.9 |
| | 11 | 71.14 | 66.45 | 0.068795 | 0.1 | 39.2 |
| | 12 | 70.78 | 67.26 | 0.06902 | 0.1 | 38.9 |
| | 13 | 67.25 | 68.22 | 0.067735 | 0.1 | 40.4 |
| | 14 | 67.44 | 67.53 | 0.067485 | 0.1 | 40.7 |
| | 15 | 67.87 | 64.05 | 0.06596 | 0.1 | 42.6 |

Unlike single-factor comparisons, this method provides a holistic statistical interpretation by integrating thermal, geometric, and microstructural indicators into one predictive framework. The proposed model is expressed as:

$$UTS = \beta 0 + \beta 1 I + \beta 2 H + \\ + \beta 3 W + \beta 4 HVWM + \epsilon \quad (3)$$

where: $I$ denotes welding current (A), $H$ is weld reinforcement height (mm), $W$ is bead width (mm), $HVWM\_\{WM\}WM$ represents weld-metal hardness (HV), and $\varepsilon$ is the error term.

Each variable represents a distinct metallurgical mechanism: heat input (I), molten-pool geometry (H and W), and microstructural strengthening (HVWM_{WM}WM).

The regression results indicated that weld-metal hardness was the most influential predictor of UTS. This finding is consistent with metallurgical principles: higher hardness typically reflects finer equiaxed grains, reduced solidification segregation, and enhanced dislocation density—traits that contribute directly to load-bearing capability. The 120 A condition, which produced the highest weld-metal hardness (43.69 HV), consequently yielded the greatest UTS (118.30 MPa). Welding current (I) emerged as the second strongest contributor. The relationship exhibited a nonlinear trend, with UTS increasing from 115

**Table 7.** Average Vickers hardness 125 A

| Current | No. | D1 (um) | D2 (um) | D (mm) | P (Kgf) | HV |
|---|---|---|---|---|---|---|
| 125 A | -15 | 67.87 | 64.05 | 0.06596 | 0.1 | 42.6 |
| | -14 | 67.44 | 67.53 | 0.067485 | 0.1 | 40.7 |
| | -13 | 67.25 | 68.22 | 0.067735 | 0.1 | 40.4 |
| | -12 | 71.14 | 66.45 | 0.068795 | 0.1 | 39.2 |
| | -11 | 70.79 | 67.27 | 0.06903 | 0.1 | 38.9 |
| | -10 | 71.29 | 71.64 | 0.071465 | 0.1 | 36.3 |
| | -9 | 72.61 | 72.57 | 0.07259 | 0.1 | 35.2 |
| | -8 | 76.42 | 73.08 | 0.07475 | 0.1 | 33.2 |
| | -7 | 74.61 | 73.29 | 0.07395 | 0.1 | 33.9 |
| | -6 | 76.04 | 73.49 | 0.074765 | 0.1 | 33.2 |
| | -5 | 74.23 | 74.233 | 0.0742315 | 0.1 | 33.4 |
| | -4 | 77.95 | 74 | 0.075975 | 0.1 | 32.1 |
| | -3 | 76.81 | 74.39 | 0.0756 | 0.1 | 32.4 |
| | -2 | 79.44 | 75.2 | 0.07732 | 0.1 | 31 |
| | -1 | 63.54 | 63.36 | 0.06345 | 0.1 | 46.1 |
| | 0 | 62.47 | 62.49 | 0.06248 | 0.1 | 47.5 |
| | 1 | 64.37 | 64.62 | 0.064495 | 0.1 | 44.6 |
| | 2 | 64.07 | 65.02 | 0.064545 | 0.1 | 44.5 |
| | 3 | 66.17 | 65.07 | 0.06562 | 0.1 | 43.1 |
| | 4 | 67.2 | 68.33 | 0.067765 | 0.1 | 40.4 |
| | 5 | 78.39 | 78.65 | 0.07852 | 0.1 | 30 |
| | 6 | 77.68 | 77.76 | 0.07772 | 0.1 | 30.7 |
| | 7 | 72.19 | 74.8 | 0.073495 | 0.1 | 34.3 |
| | 8 | 76.24 | 74.82 | 0.07553 | 0.1 | 32.5 |
| | 9 | 77.52 | 76.67 | 0.077095 | 0.1 | 31.2 |
| | 10 | 73.75 | 74.79 | 0.07427 | 0.1 | 33.6 |
| | 11 | 66.43 | 65.54 | 0.065985 | 0.1 | 39.2 |
| | 12 | 71.14 | 66.45 | 0.068795 | 0.1 | 39.7 |
| | 13 | 70.79 | 65.27 | 0.06803 | 0.1 | 40.7 |
| | 14 | 70.14 | 65.45 | 0.067795 | 0.1 | 41.4 |
| | 15 | 67.20 | 66.33 | 0.066765 | 0.1 | 42.9 |

A to 120 A but declining at 125 A. This behaviour reflects the transition from insufficient heat input (115 A) to optimal melting and fusion (120 A), followed by mild overheating and grain coarsening at 125 A. Bead width (W) showed a negative correlation with UTS, suggesting that excessively wide beads – common at higher heat inputs – tend to produce slower cooling rates, enlarged HAZs, and coarser grain structures, thereby reducing tensile efficiency. Conversely, reinforcement height (H) demonstrated a modest positive contribution, indicating that adequate metal deposition and pool stability can improve fusion quality, albeit with less dominance than microstructural factors. Collectively, the regression model confirms that the 120 A condition lies near the optimum welding window, where heat input, bead geometry, and microstructural refinement are best balanced. These findings validate experimental trends and provide a quantitative foundation for future parameter optimisation strategies. Recent studies on aluminium alloys similarly emphasise the

**Table 8.** Average Vickers hardness for each zone

| Zone | 115 A | 120 A | 125 A |
|---|---|---|---|
| BM | 39.10 | 40.67 | 39.63 |
| HAZ | 32.97 | 34.53 | 32.76 |
| WM | 38.98 | 43.69 | 40.19 |

**Note:** Processed data (2025).

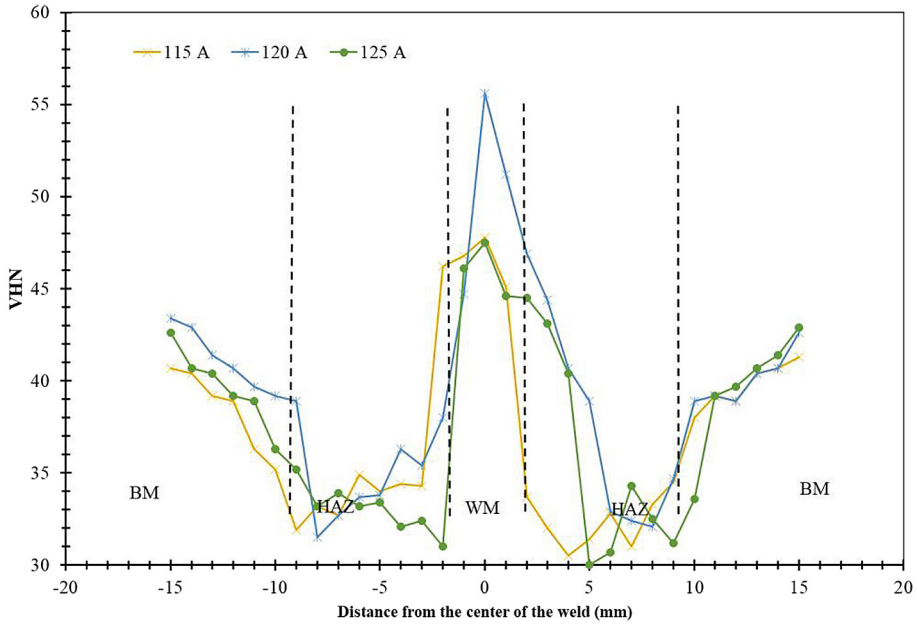


**Figure 9.** Graph of hardness values of the current variation

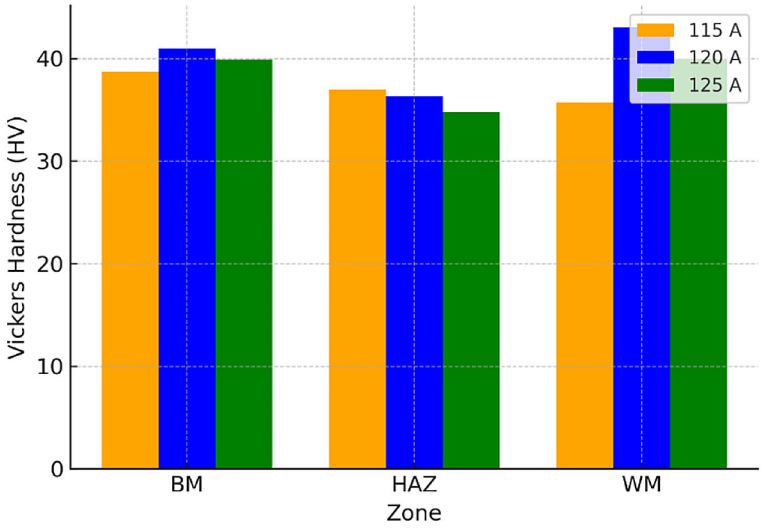


**Figure 10.** Hardness value comparison bar chart

synergy among heat input, bead morphology, and microstructural gradients in predicting mechanical performance [34].

Although the present investigation used a square butt joint, an examination of groove geometry is essential, as the weld-joint configuration profoundly influences thermal flow, penetration depth, molten-pool dynamics, and final mechanical performance. Numerous studies on aluminium welding highlight that groove design is as critical as welding current or travel speed in determining weld quality [35]. For thin AA8011 sheets (3 mm), the square butt joint is generally the most practical option. It requires minimal machining, limits heat input, and reduces the potential for distortion – an essential consideration for lightweight radiator components where geometric stability is crucial. The results of this study support that choice: the 120 A condition achieved full penetration, stable bead morphology, and superior tensile performance without requiring bevel preparation.

In contrast, V-groove joints are typically employed for thicker aluminium plates. Their bevel angle promotes deeper penetration and improved access for root fusion, especially

in single-sided operations. However, for thin sheets, V-grooves impose unnecessary thermal loads, broaden the HAZ, and increase the risk of warping – effects that would be detrimental to AA8011, which is highly sensitive to thermal softening. U-groove joints, known for their smooth molten-metal flow and lower stress concentration at the root, are best suited for heavy-section aluminium welding. While they provide excellent weld morphology, their geometric complexity increases heat accumulation inside the groove, which is undesirable for thin materials. Excess heat may lead to microstructural coarsening, increased porosity, and reduced mechanical uniformity across the weld zone. The findings of this study show that a simple square butt configuration, when combined with an optimised welding current (120 A), already achieves ideal penetration, minimal distortion, and refined weld-metal microstructure. Therefore, groove modification would offer limited benefit at this thickness. Nevertheless, future research should expand toward evaluating groove geometry effects on AA8011 in thicker sections (>5 mm), where heat flow and penetration challenges become more significant. Coupling experimental approaches with computational thermal-cycle models – such as finite-element heat-transfer simulations – would provide deeper insights into groove-dependent thermal gradients, cooling rates, and microstructural evolution.

## CONCLUSIONS

This study investigated the influence of TIG welding current on the mechanical response, hardness distribution, bead geometry, and microstructural evolution of AA8011 aluminium alloy, which is widely used in automotive radiator applications, yet remains insufficiently documented in the welded condition. The findings demonstrate that welding current plays a decisive role in controlling the thermal cycle and structural integrity of the welded joint.

The optimum current parameter is 120 A, which produced:

- the highest tensile performance (UTS = 118.30 MPa; YS = 79.68 MPa),
- the highest weld metal hardness (43.69 HV),
- the most refined and homogeneous grain structure in the weld metal,
- and the least softening in the HAZ.

Currents below 120 A (115 A) resulted in insufficient heat input, incomplete fusion, a smaller reinforcement area, and reduced mechanical strength despite higher ductility. Conversely, higher heat input (125 A) caused partial grain coarsening and decreased strength compared to the 120 A condition.

This research provides the first integrated dataset combining tensile performance, hardness mapping, weld-bead geometry, and microstructural characterisation for TIG-welded AA8011 aluminium alloy. Unlike previous studies that focused primarily on the AA5xxx and AA6xxx series, the present work bridges a significant knowledge gap by establishing quantitative relationships between welding current and post-weld mechanical properties of AA8011, supported by multivariate regression modelling. These results provide a scientific foundation for optimising TIG welding parameters for 8xxx-series lightweight alloys in radiator and heat-exchanger applications.

The findings demonstrate that proper selection of welding current is critical for maximising weld integrity in AA8011 alloy. The results serve as a reference for manufacturing industries that employ TIG welding for aluminium radiator components, enabling improved structural performance, reliability, and long-term durability.

Future research should expand the optimisation framework by incorporating:

1. Weld groove geometry variations (V-groove, U-groove, and modified butt joints),
2. Advanced parameter optimisation algorithms, such as RSM, TLBO, genetic algorithms, or neural-network-based prediction models,
3. Thermal-cycle monitoring to strengthen correlations between heat input and microstructural evolution,
4. Corrosion testing for radiator-specific operating environments.

These expanded efforts will enable a more comprehensive understanding of TIG welding behaviour in AA8011 alloy and enhance its application potential in automotive thermal systems.

### Acknowledgments

The authors express sincere gratitude to the Department of Mechanical Engineering, Diponegoro University (UNDIP), for providing academic guidance and access to the laboratory throughout

this research. Appreciation is also extended to the Department of Maritime Affairs, Samarinda State Polytechnic (POLNES), for granting research facilities, material support, and administrative permission. The valuable contributions, technical assistance, and constructive feedback from colleagues and supervisors are deeply acknowledged. This work is expected to advance welding science and aluminium engineering applications, particularly in lightweight automotive heat–exchange systems.

## REFERENCES

1. Wang L. et al., A novel heterogeneous multi-wire indirect arc directed energy deposition for in-situ synthesis Al-Zn-Mg-Cu alloy: Process, microstructure and mechanical properties, Addit Manuf, 2023; 72: 103639, https://doi.org/10.1016/j.addma.2023.103639
2. Brezinová J. et al., Possibilities of repairing functional surfaces of Molds for injecting al alloys using manual GTAW cladding, Metals (Basel), Oct. 2022; 12(11): 1781, https://doi.org/10.3390/met12111781
3. Ahmed S. et al., Optimization of process parameters in friction stir welding of aluminum 5451 in marine applications, J Mar Sci Eng, 2022; 10(10), https://doi.org/10.3390/jmse10101539
4. Su C. Q., Wang S., Liu X., Tao Q., and Wang Y. P., Experimental and numerical investigation on spray cooling of radiator in fuel cell vehicle, Energy Reports, 2022; 8: 1283–1294, https://doi.org/10.1016/j.egyr.2021.11.174
5. Liu Y. et al., Process analysis and multi-parameter optimization of 5052 aluminum alloy FSW based on thermo-mechanical coupling and Taguchi method, Sci Rep, 2025; 15(1): 1–17, https://doi.org/10.1038/s41598-024-82923-5
6. Liu M., Wang W., Zhang M., and Qiu Y., Effect of heat treatment on the microstructure and mechanical properties of Mg-3.4Y-3.6Sm-2.6Zn-0.8Zr alloy, Xiyou Jinshu Cailiao Yu Gongcheng/Rare Metal Materials and Engineering, 2019; 48(7): 2056–2061.
7. Karagöz Y., Köten H., Tunçer E., and Pusat Ş., Effect of $Al_2O_3$ addition to an internal combustion engine coolant on heat transfer performance, Case Studies in Thermal Engineering, 2022; 31: 1–10, https://doi.org/10.1016/j.csite.2022.101847
8. Arif M., Kumam P., Kumam W., and Mostafa Z., Heat transfer analysis of radiator using different shaped nanoparticles water-based ternary hybrid nanofluid with applications: A fractional model, Case Studies in Thermal Engineering, 2022: 31(January): 101837, https://doi.org/10.1016/j.csite.2022.101837
9. Sivalingam V., Ganesh Kumar P., Prabakaran R., Sun J., Velraj R., and Kim S. C., An automotive radiator with multi-walled carbon-based nanofluids: A study on heat transfer optimization using MCDM techniques, Case Studies in Thermal Engineering, December 2022; 29: 101724, https://doi.org/10.1016/j.csite.2021.101724
10. Hayat F., Electron beam welding of 7075 aluminum alloy: Microstructure and fracture properties, Engineering Science and Technology, an International Journal, 2022; 34: 101093, https://doi.org/10.1016/j.jestch.2022.101093
11. Ghumman K. Z., Ali S., Din E. U., Mubashar A., Khan N. B., and Ahmed S. W., Experimental investigation of effect of welding parameters on surface roughness, micro-hardness and tensile strength of AISI 316L stainless steel welded joints using 308L filler material by TIG welding, Journal of Materials Research and Technology, 2022; 21: 220–236, https://doi.org/10.1016/j.jmrt.2022.09.016
12. Assefa A. T. et al., Experimental investigation and parametric optimization of the tungsten inert gas welding process parameters of dissimilar metals, Materials, 2022; 15(13), https://doi.org/10.3390/ma15134426
13. Li Y., Zong R., Zhang Y., and Yao J., Research status and prospects for tig-mig hybrid-arc-welding technology, Materiali in Tehnologije, 2024; 58(3): 387–396, https://doi.org/10.17222/mit.2023.974
14. Peng J. et al., Revealing the microstructure evolution, deformation behavior and tensile properties of AZ31/AM60 dissimilar Mg alloy joints under different welding technologies, Journal of Materials Research and Technology, 2024; 28(1November 2023): 814–830, https://doi.org/10.1016/j.jmrt.2023.11.282
15. Arun Kumar R., Vaira Vignesh R., Srirangarajalu N., and Padmanaban R., Examination of the mechanical, corrosion, and tribological behavior of friction stir welded aluminum Alloy AA8011, Transactions on Maritime Science, 2021; 10(1): 20–41, https://doi.org/10.7225/toms.v10.n01.002
16. Kailainathan S., Ezhilan M., Alagarsamy S. V., and Chanakyan C., Investigations on tribological behaviour of titanium dioxide particles filled Al-0.6Fe-0.5Si alloy composite using topsis approach, Archives of Metallurgy and Materials, 2023; 68(4): 1429–1438, https://doi.org/10.24425/amm.2023.146209
17. Lakshmi A. A. et al., Friction stir welding of aluminum AA6061 & AA8011 using optimization approach based on both Taguchi and grey relational analysis, Cogent Eng, 2024; 11(1), https://doi.org/10.1080/23311916.2024.2393737
18. Kotadia H. R., Franciosa P., Jabar S., and Ceglarek

D., Remote laser welding of Zn coated IF steel and 1050 aluminium alloy: processing, microstructure and mechanical properties, Journal of Materials Research and Technology, 2022; 19: 449–465, https://doi.org/10.1016/j.jmrt.2022.05.041

19. Mustafa S., Haider J., Matteis P., and Murtaza Q., Synthesis and wear behaviour analysis of SiC- and rice husk ash-based aluminium metal matrix composites, Journal of Composites Science, 2023; 7(9): 1–15, https://doi.org/10.3390/jcs7090394
20. Han L., Han T., Wu Q., Xu S., Sun J., and Wang Y., Study on microstructural characterization and local stress–strain behavior of transition zone within K-TIG welded SAF2205/Q235 dissimilar joints, Journal of Materials Research and Technology, 2023; 24: 5119–5138, https://doi.org/10.1016/j.jmrt.2023.04.112
21. Andoor P. A., Okeoma K. B., and Mbamara U. S., Adsorption inhibitive properties of *Rosmarinus officinalis* L. on aluminium AA8011 Alloy in 1.0M HCl, Materials Protection, 2023; 64(2): 204–212, https://doi.org/10.5937/zasmat2302204A
22. Habba M. I. A. et al., Comparative study of FSW, MIG, and TIG Welding of AA5083-H111 based on the evaluation of welded joints and economic aspect, Materials, 2023; 16(14): 5124, https://doi.org/10.3390/ma16145124
23. Yelamasetti B. et al., Optimization of TIG welding process parameters using Taguchi technique for the joining of dissimilar metals of AA5083 and AA7075, Sci Rep, 2024; 14(1): 1–21, https://doi.org/10.1038/s41598-024-74458-6
24. Iremia S., Okechukwu I., and Otanocha O., Parametric analysis and optimization of TIG welding for enhanced structural integrity of mild-steel Sktm13a pipe butt joints, International Journal of Mechanical Engineering and Applications, 2025; 13(1): 27–52, https://doi.org/10.11648/j.ijmea.20251301.12
25. Fouad R. A. et al., Comparative analysis of filler metals on microstructure and mechanical performance of TIG-welded AISI 201 austenitic stainless steel joints, Science and Technology of Welding and Joining, 2024; 29(5–6): 356–367, https://doi.org/10.1177/13621718241283374
26. Riswanda, Akhyar, H. Kadir, Sugianto, and Saragih A. D., The effect of heat input on tensile strength, Vickers hardness, and microstructure on DMW of AISI 1015 and 304L SS through the GMAW process, Journal of Achievements in Materials and Manufacturing Engineering, 2024; 123(1): 5–16, https://doi.org/10.5604/01.3001.0054.4920
27. Shete H. and Powar V., Effects of welding parameters on mechanical properties and microstructure of TIG welded joints of AA4043, J Phys Conf Ser, 2023; 2604(1): 0–13, https://doi.org/10.1088/1742-6596/2604/1/012005
28. Wang L., Liu Z., Feng Y., Fu Y. K., Zhao S., and Guo E., Effect of TIG repaired welding process on microstructure and mechanical properties of as-cast Mg-4Y-3Nd-1.5Al alloy, Mater Charact, 2025; 219(July 2024): 114622, https://doi.org/10.1016/j.matchar.2024.114622
29. Mohsein Z. H., Abdulwahhab A. B., and Abbas A. M., Study effect of active flux on mechanical properties of TIG welding process, Results in Engineering, 2025; 26(February): 104681, https://doi.org/10.1016/j.rineng.2025.104681
30. Baghel P. K., Parameter optimization of pulse current gas tungsten arc welding process using teaching learning based optimization and cuckoo search algorithm, Discover Mechanical Engineering, 2025; 4(1), https://doi.org/10.1007/s44245-025-00120-8
31. Shafeek M., Suranjan S., Doreswamy D., and Sachidananda H. K., Effect of welding parameters on microstructure and mechanical properties of GMAW welded S275 steel welded zone, Discov Mater, 2024; 4(1), https://doi.org/10.1007/s43939-024-00169-4
32. Ramarajan A. and Jayakumar K., Influence of pulsed TIG welding process parameters on the mechanical characteristics of AA5083 with AA6082 weldments, Mater Res Express, Feb. 2023; 10(2): 026504, https://doi.org/10.1088/2053-1591/acb682
33. Dada M. and Popoola P., Recent advances in joining technologies of aluminum alloys: a review, vol. 4, no. 1. Springer International Publishing, 2024. https://doi.org/10.1007/s43939-024-00155-w
34. Wang Y. et al., Prediction of internal welding penetration based on IR thermal image supported by machine vision and ANN-model during automatic robot welding process, Journal of Advanced Joining Processes, 2024; 9(February): 100199, https://doi.org/10.1016/j.jajp.2024.100199
35. Song G., Xu Z., Lang Q., Liu X., Wang H., and Liu L., A laser-induced TIG arc narrow-gap welding technique for TC4 titanium alloy thick plates based on the spatial position control of laser, arc and filler wire, Metals (Basel), 2024; 14(5), https://doi.org/10.3390/met14050510